Physica B 615 (2021) 413061

Contents lists available at ScienceDirect

Physica B: Physics of Condensed Matter

journal homepage: www.elsevier.com/locate/physb

Structural, elastic, vibrational, electronic and optical properties of $SmFeO_3$ using density functional theory

Shahran Ahmed [a], Sadiq Shahriyar Nishat [b], Alamgir Kabir [b], A.K.M. Sarwar Hossain Faysal [a], Tarique Hasan [a], Shovon Chakraborty [a], Imtiaz Ahmed [a,*]

[a] *Department of Electrical and Electronic Engineering, University of Dhaka, Dhaka, 1000, Bangladesh*
[b] *Department of Physics, University of Dhaka, Dhaka, 1000, Bangladesh*

ARTICLE INFO

Keywords:
$SmFeO_3$
Local and semilocal density functionals
Hubbard-U Corrected functional
Modified Becke-Johnson potential
Heyd–Scuseria–Ernzerhof density functional
Density functional perturbation theory

ABSTRACT

We perform first principles simulations for the structural, elastic, vibrational, electronic and optical properties of orthorhombic samarium orthoferrite $SmFeO_3$ within the framework of density functional theory. A number of different density functionals, such as local density approximation, generalized gradient approximation, Hubbard interaction modified functional, modified Becke-Johnson approximation and Heyd–Scuseria–Ernzerhof hybrid functional have been used to model the exact electron exchange-correlation. We estimate the energy of the ground state for different magnetic configurations of $SmFeO_3$. Its crystal structure is characterized in terms of calculated lattice parameters, atomic positions, relevant ionic radii, bond lengths, bond angles and compared with experimental values. The stability of its orthorhombic structure is simulated in terms of elastic properties. The vibrational phonon modes are calculated using density functional perturbation theory and are shown to be consistent with recent experimental observations. In case of electronic properties, we provide estimates based on density functionals with varying degrees of computational complexities in the Jacob's ladder. We show Heyd–Scuseria–Ernzerhof density functional theory provides better modelling for localized *d* and *f* orbitals in SFO which is in line with theoretical work on other rare-earth materials. The linear optical properties in terms of complex dielectric function and other standard optical functions are derived for Hubbard corrected generalized gradient approximation in combination with Fermi's golden rule.These provide a good theoretical analysis of structural, elastic, vibrational, electronic and optical properties of SFO.

1. Introduction

The rare-earth orthoferrites managed to reign in the active field of materials research for more than half a century [1]. These materials have common chemical formula $RFeO_3$ where R is a rare-earth ion in the lanthanide series. Originally $RFeO_3$ materials were studied as a family of canted anti-ferromagnets which revealed exciting, novel; sometimes baffling magnetic properties [2–4]. One of the prominent members of the rare-earth orthoferrites is the samarium orthoferrite $SmFeO_3$ (SFO hereafter). SFO is a promising candidate for many spintronic device applications for many of its interesting and intriguing properties; such as spontaneous reversal at cryogenic temperatures below 4 K, fast magnetic switching capabilities with high spin switching temperature of 278.5 K and high spin axis rotation temperature of 480 K [5]. The magnetic properties of SFO depend on particle size, surface morphology and measurements temperature [6–10]. Its high magnetostriction coefficient along with the anomalous magneto-electric behavior may open up possibilities for different magnetoelastic devices [11–13].

SFO has also found its applications in high performance electrode materials for solid state lithium-ion batteries [14], as good dielectric materials for electronics [15,16], in photocatalytic applications for renewable energy technology [17,18] and also in multiferroics [19,20]. A material with such diverse applications also embodies rich physics due to its bewildering exchange interaction between the 4*f* electrons in the rare-earth Sm and 3*d* electrons in transition element Fe. This prompted the need for understanding this fascinating material from quantum mechanical first principles calculations within the framework of density functional theory (DFT) [21,22]. The DFT based simulations in combination with experimental observations opened up fascinating debate about the origin (complex interplay between the inverse Dzyaloshinskii-Moriya and exchange-striction) and existence of ferroelectric ordering in SFO [23–26]. The SFO vibrational phonon

---

[*] Corresponding author.
E-mail address: imtiaz@du.ac.bd (I. Ahmed).

https://doi.org/10.1016/j.physb.2021.413061
Received 24 December 2020; Received in revised form 18 February 2021; Accepted 11 April 2021

frequencies and associated Raman modes have been studied using DFT simulations along with experimental investigations [27–30]. The DFT based simulations have been performed to understand electronic properties of a number of $R\mathrm{FeO}_3$ materials including SFO, where the presence of $4f$ electrons in Sm caused difficulties in predicting correct electronic ground state configuration [31,32]. An improved electronic band structure calculation of SFO based on Hubbard interaction corrected functionals gave better estimates for the experimentally measured electronic properties of SFO [33].

Numerous experimental work on SFO exist in literature exploring its physical properties and discovering its potential in many applications. Although a large number of theoretical work have been undergone in many different rare-earth orthoferrites, to the best of our knowledge, detail theoretical analysis for elastic, vibrational, electronic and optical properties of SFO are hard to find in existing studies. Here we perform DFT simulations to investigate these properties and compared the results with available experimental observations. We explore different density functionals with varying degrees of computational complexities within the DFT framework to make a comparative analysis and study their potentials in explaining the relevant physical properties of SFO. We found that Hubbard corrected generalized gradient approximations provide satisfactory estimates for the above-mentioned properties of SFO. In case of electronic properties, we show that the localized $3d$ and $4f$ orbitals in SFO can be described using modified Becke-Johnson and hybrid functional with increased computational complexities; without relying on judicious choice of the Hubbard interaction parameter.

2. Computational details

We perform DFT based spin-polarized and non spin-polarized simulations within the framework projector augmented wave (PAW) method using the Vienna *Ab Initio* Simulation Package (VASP) [34,35]. We consider a unit cell of SFO which consists of four Sm atoms, four Fe atoms and twelve O atoms; a total of 20 atoms are considered for all simulations performed in this paper. For the PAW, we divide the SFO electron configuration into core and valence categories. We considered sixteen electrons of Sm ($4f^5 5s^2 5p^6 5d^1 6s^2$), 8 electrons of Fe ($3d^6 4s^2$) and six electrons of O ($2s^2 2p^4$) as valence electrons (in total 30 valence electrons) and the remaining electrons are treated within the frozen core approximation. Structural relaxation and optimization are carried out by sampling the Brillouin zone (BZ) with a 5 × 5 × 3 Monkhorst Pack grid k-points mesh until the Hellmann–Feynman forces reached 0.005 eV/Å. We used the self-consistent total energy convergence of 10^{-8} eV. For truncating the plane wave expansion for the PAW, a plane wave energy cutoff of 480 eV is used in all simulations; except for the case of elastic and vibrational properties where an increased energy cutoff of 520 eV is used to ensure convergence.

We used a number of different approximations for the unknown exchange-correlation term in the Kohn-Sham Hamiltonian [36]. We use Ceperley-Alder local density approximation (LDA) where the exchange term is obtained from the homogeneous electron gas and the correlation term is approximated from numerically accurate Monte Carlo methods [37]. The semi local generalized gradient approximation (GGA) is implemented with three different standard variants Perdew-Wang (PW91) [38], Perdew-Burke-Ernzerhof (PBE) [39] and its optimized version PBEsol [40]. We also make use of the “Hubbard-U″ scheme for LDA and GGA-PBE which are referred to as LDA + U and GGA-PBE + U [41,42]. A number of different values for the Hubbard parameter U within the energy range [1 eV, 8 eV] have been tested during the structural relaxation process to find the best match with the experimental structural parameters presented in Table 2. Weber *et al.* used $U =$ 4 eV for a number of rare-earth ortho ferrites and showed good agreement with experimentally obtained structural parameters and Raman modes [27]. In other places, treating the transition and rare earth element with different U seems to provide good estimates for magnetic properties [33,43,44]. Here we used U = 6 eV for Sm and U = 4 eV for Fe atoms to boost the dilute Coulomb interaction for the localized orbitals. These are consistent with the choices for the on-site Coulomb interaction term U in case of rare-earth and transition metal atoms that produce correct materials properties [22,27,33,45,46]. We also explore the modified Becke and Johnson (mBJ) exchange potential in combination with GGA-PBE in case of electronic properties simulations [47]. For more accurate estimations for electronic properties, computationally intense Heyd–Scuseria–Ernzerhof (HSE06) hybrid functional based simulations have been performed [48–50].

The SFO can exist in four different magnetic structures; one ferromagnetic (FM) and three antiferromagnetic (AFM) which are A-AFM, C-AFM and G-AFM, see Fig. 1(a–d). We have calculated total energies for all four magnetic configurations for LDA + U, GGA-PBE and GGA-PBE + U functionals. In all cases, G-AFM turned out to be the magnetic configuration with minimum total energy which is consistent with results in Refs. [26,31,32]. Assuming the G-AFM as our minimum energy reference, we estimate the energy differences $\Delta E_{\mathrm{FM-GAFM}}$, $\Delta E_{\mathrm{AAFM-GAFM}}$ and $\Delta E_{\mathrm{CAFM-GAFM}}$ for the three higher energy states FM, A-AFM and C-AFM respectively, see Table 1. All spin-polarized calculations presented in this article are for G-AFM magnetic configuration in SFO.

3. Crystal structure

The SFO has a distorted orthorhombic perovskites unit cell structure with the space group *Pbnm* (no. 62) at room temperature where the magnetic easy axis is along c axis of the orthorhombic unit cell [18,26,31,32,51]. Each unit cell ($a < b < c$) of SFO has four Sm^{3+} ions at the centers and four Fe^{3+} at the corners surrounded by oxygen octahedra which are tilted along the crystallographic b-axis, see Fig. 1 (a). The orthorhombic structural distortion is due to the size mismatch between the octahedral holes available for the Sm^{3+} in the unit cell and the actual smaller Sm^{3+} ion.

The SFO has experimentally measured mutually orthogonal $(\alpha = \beta =$

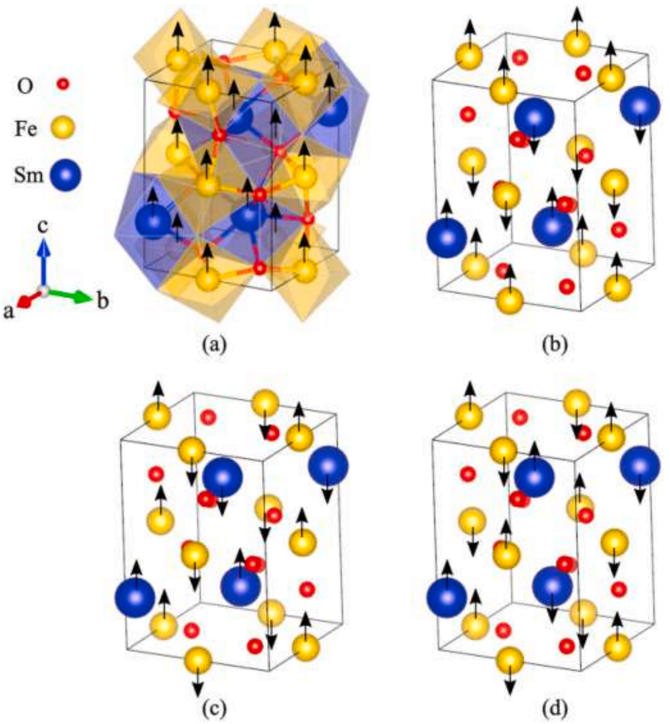

Fig. 1. The SFO unit cell with four different spin magnetic configurations, (a) Ferromagnetic (FM), (b) A-type antiferromagnetic (A-AFM), (c) C-type antiferromagnetic (C-AFM) and (d) G-type antiferromagnetic (G-AFM). Black arrow indicates the spin magnetic moment orientations of atoms.

Table 1

Energy differences between different SFO magnetic configurations calculated for LDA + U, GGA-PBE and GGA-PBE + U.

Method	LDA + U	GGA-PBE	GGA-PBE + U
$\Delta E_{FM\text{-}GAFM}$ (eV)	1.219	1.063	0.828
$\Delta E_{AAFM\text{-}GAFM}$ (eV)	1.5	7.001	0.575
$\Delta E_{CAFM\text{-}GAFM}$ (eV)	0.726	0.13	0.220

γ = 90 deg) lattice constants a = 5.39 Å, b = 5.58 Å, c = 7.71 Å with a unit cell volume V = 231.89 Å^3 [3,14,18,30]. We performed structural optimization of the unit cell with different variants of LDA and GGA in both spin-polarized and non-spin-polarized configurations. The simulated values for lattice parameters a, b, c, V, α, β and γ are summarized in Table 2. For non-spin-polarized calculations, all variants of LDA and GGA show significant deviations resulting in poor estimates for lattice parameters as compared to experimental values. Lattice parameters calculated from GGA-PW91 functional produced inconsistent values compared to experimental results even in the case of spin-polarized calculations. The basic LDA provides more reasonable estimates for lattice parameters in the spin-polarized configuration. Moreover LDA + U, GGA-PBE and GGA-PBE + U also provide good estimation for lattice parameters in case of spin-polarized calculations. Both GGA-PBE and GGA-PBE + U consistently overestimated the unit cell volume V by 1.34% and 2.77% respectively whereas LDA + U under estimate it by 4.12%. This is consistent with the fact that LDA usually over binds the atoms inside the unit cell and the semi local GGA does the opposite. Based on these reliable estimates, we calculate the atomic positions of four Sm^{3+}, four Fe^{3+} and twelve O^{2-} ions in the unit cell using Wyckoff coordinates [51,52], see Table 3. For example after internal GGA-PBE + U structure relaxation, the Sm atom occupies the (0.9852, 0.0591, 0.2503) site, the Fe atom in (0.0000, 0.4994, 0.0000) site, the O1 atom in the (0.6997, 0.2994, 0.0503) site, and the O2 atom in (0.0959, 0.4696, 0.2499) sites in Wyckoff coordinates which are in good agreement with experimentally measured values obtained from Rietveld refinement [3,14,18,30]. We calculate ionic radius, bond lengths and bond-angles relevant for SFO, see Table 4 [18,53,54] and compared with experimental values. Three GGA-PBE + U optimized Sm–O bond lengths are 2.33, 2.40, 2.73 Å (in case of LDA + U, 2.28, 2.51, 2.65 Å) are slightly larger than the Fe–O bond lengths of 2.015, 2.027, 2.051 Å (in case of LDA + U, 1.96, 1.980, 2.00 Å). The distances between Sm^{3+} and Fe^{3+} ions are 3.16, 3.29 and 3.71 Å for GGA-PBE + U (3.088, 3.21, 3.341 Å in case of LDA + U). The bond angles of Fe–O–Sm are 85.789°, 89.785°, 89.953° in GGA-PBE + U relaxed structure (85.76°, 86.03°, 90.21° for LDA + U), deviating from the ideal value of 90°. For the undistorted orthorhombic perovskites unit cell with space group *Pbnm*, symmetry defines the positions of atoms as such the Sm-Fe-O bond angles are 90° [51]. But during the structural relaxation process atoms rearrange their positions which distorts ideal orthorhombic configuration leading to deviation of the Sm-Fe-O bond angles from 90° [52,55].

Table 4

Calculated ionic radii, Sm–O, Fe–O, Sm–Fe bond lengths, Fe–O-Sm, Fe–O–Fe and O–Fe–O bond angles for spin-polarized LDA + U, GGA-PBE and GGA-PBE + U. The corresponding experimental values (Exp.) are taken from the Refs. [18,30,62].

Parameter	LDA + U	GGA-PBE	GGA-PBE + U	Exp.
Ionic Radius (Å)	Sm = 1.482	Sm = 1.482	Sm = 1.482	Sm = 0.96
	Sm = 1.482 O = 0.82	Fe = 1.302 O = 0.82	Fe = 1.302 O = 0.82	Fe = 0.55 O = 1.4
d_{Sm-O} (Å)	2.28, 2.51, 2.65	2.33, 2.43, 2.65	2.33, 2.40, 2.73	2.4029
d_{Fe-O} (Å)	1.96, 1.98, 2.00	1.98, 2.00, 2.10	2.015, 2.027, 2.051	2.0093
d_{Sm-Fe} (Å)	3.088, 3.21, 3.341	3.15, 3.30, 3.38, 3.66	3.16, 3.29, 3.71	3.4091
$\Theta_{Fe-O-Sm}$ (deg.)	85.76, 86.03, 90.21	87.77, 88.82, 90.62	85.789, 89.785, 89.953	–
$\Theta_{Fe-O-Fe}$ (deg.)	149.39	148.61, 149.61, 150.00	148.433, 148.440, 148.597	149.9356
Θ_{O-Fe-O} (deg.)	88.57, 89.27, 90.86	87.70, 88.92, 90.43	88.41, 89.797, 90.012	–

Table 2

Structural lattice parameter of SFO calculated from LDA, LDA + U, GGA-PW91, GGA-PBE, GGA-PBE + U and GGA-PBEsol for both spin-polarized and non spin-polarized configurations. The experimental (Exp.) lattice parameter values can be found in Refs. [3,14,18,30].

Lattice Parameters										
Methods	Spin-Polarized							Non-Spin-Polarized		
	a (Å)	b (Å)	c (Å)	V (Å^3)	$\alpha = \beta = \gamma$ (deg.)	a (Å)	b (Å)	c (Å)	V (Å^3)	$\alpha = \beta = \gamma$ (deg.)
LDA	5.203	5.277	7.392	202.96	90	4.972	5.484	7.238	197.35	90
LDA + U	5.301	5.529	7.586	222.34	90	5.134	5.448	7.298	204.12	90
GGA-PW91	2.574	10.953	9.443	266.23	90	7.543	4.574	8.876	306.23	90
GGA-PBE	5.436	5.648	7.654	234.99	90	5.125	5.590	7.397	211.91	90
GGA-PBE + U	5.428	5.657	7.761	238.31	90	5.317	5.540	7.516	221.39	90
GGA-PBEsol	5.258	5.285	7.438	206.69	90	5.063	5.579	7.185	202.95	90
Exp.	a = 5.39 Å		b = 5.58 Å		c = 7.71 Å			V = 231.89 Å^3		$\alpha = \beta = \gamma = 90$

Table 3

Atomic positions of Sm, Fe and O atoms in SFO unit cell in terms of Wyckoff coordinates calculated from LDA + U, GGA-PBE and GGA-PBE + U for G-AFM spin-polarized configuration. The corresponding experimental values (Exp.) are taken from the Refs. [18,30,62].

Atomic Positions in Wyckoff Coordinate													
		LDA + U			GGA-PBE			GGA-PBE + U			Exp.		
Atom	Site	x	y	z	x	y	z	x	y	z	x	y	z
Sm	4a	0.9854	0.0592	0.2507	0.9897	0.0548	0.2506	0.9852	0.0591	0.2503	0.9881	0.0531	0.2502
Fe	4b	0.0000	0.4966	0.0000	0.0000	0.4966	0.0005	0.0000	0.4994	0.0000	0.0000	0.5000	0.0000
O1	8d	0.7001	0.2982	0.0487	0.6982	0.3049	0.0452	0.6997	0.2994	0.0503	0.7151	0.2509	0.0557
O2	4c	0.0930	0.4735	0.2498	0.0902	0.4735	0.2499	0.0959	0.4969	0.2499	0.1040	0.4033	0.2500

4. Elastic properties

To investigate the structural stability of the G-AFM orthorhombic SFO, we calculated elastic tensor C_{ij} by applying forces thereby creating six finite perturbation to the lattice and measuring the C_{ij} from the standard strain-stress relationship [56,57]. To ensure the convergence of the stress tensor we use the plane wave energy cutoff to be 520 eV for the PAW. For orthorhombic SFO, we have six non-zero independent elastic constants C_{11}, C_{12}, C_{13} , C_{22} , C_{23} , C_{33} , C_{44} , C_{55} and C_{66}. From these non-zero $C_{ij}s$, we can check the necessary and sufficient Born criteria for mechanical stability for an orthorhombic system

$$C_{11} > 0,\ C_{44} > 0,\ C_{55} > 0,\ C_{11}C_{22} > \ C_{12}^2 \tag{1}$$

$$C_{11}C_{22}C_{33} + 2C_{12}C_{13}C_{23} - C_{11}C_{23}^2 - C_{22}C_{13}^2 - C_{33}C_{12}^2 > 0 \tag{2}$$

are satisfied in all three cases, i.e., LDA, LDA + U and GGA-PBE + U [58], see Table 5. The other important elastic properties like bulk-modulus (B), shear modulus (G), Young's modulus (E), Poisson's ratio (ν) are calculated using three different theories such as Reuss (B_R, G_R, E_R, ν_R), Voigt (B_V, G_V, E_V, ν_V) and Hill (B_H, G_H, E_H, ν_H) [59–61].

We note that the values for Voigt–Reuss–Hill bulk moduli are different for the orthorhombic unit cell indicating the departure from the cubic symmetry (they are equal only for unit cell with cubic symmetry). The LDA predicts the highest values for shear modulus (G_H = 82.881 GPa) and Young's modulus (E_H = 193.048 GPa) as compared to LDA + U and GGA-PPE + U. This implies both resistance to plastic deformation and stiffness of SFO are largest within the LDA exchange-correlation framework. This is indicative of atoms in SFO unit cell being over bounded in LDA. The Hubbard U term in case of LDA + U corrects for the binding energies of atoms in SFO unit cell which results in reduction of both G_H and E_H to 69.627 GPa and 183.656 GPa respectively. In case of GGA-PBE + U, the values for G_H and E_H reduces even further to 55.810 GPa and 146.477 GPa bearing the signature of under bounded atoms in the unit cell.

For ductile/brittle test, the estimated Pugh ratio for LDA, LDA + U and GGA-PBE + U are 0.864, 0.412 and 0.429 respectively; all of which are smaller than the critical value of 1.75 indicating the brittle nature of orthorhombic SFO [63]. This is corroborated with the estimated values of Poisson's ratio (ν_V, ν_R and ν_H) being smaller than the critical value of 0.33 in the Voigt–Reuss–Hill framework.

Table 5
Elastic constant (C_{ij}), bulk modulus (B_V, B_R and B_H), shear modulus (G_V, G_R and G_H), Young's modulus (E_V, E_R and E_H), Poisson's ratio (ν_V, ν_R and ν_H)) in Voigt-Reuss-Hill framework for G-AFM orthorhombic SFO using LDA, LDA + U and GGA-PBE + U.

Elastic Properties	Spin-Polarized		
	LDA	LDA + U	GGA-PBE + U
C_{11} (GPa)	211.923	288.021	181.250
C_{12} (GPa)	63.803	96.286	96.419
C_{13} (GPa)	58.391	151.939	75.115
C_{22} (GPa)	143.286	215.376	223.149
C_{23} (GPa)	25.618	132.203	121.135
C_{33} (GPa)	237.943	293.781	199.397
C_{44} (GPa)	98.739	96.396	84.671
C_{55} (GPa)	85.035	82.377	68.517
C_{66} (GPa)	93.821	44.923	35.920
B_V (GPa)	98.753	173.115	132.126
B_R (GPa)	93.110	164.829	127.968
B_H (GPa)	95.931	168.972	130.047
G_V (GPa)	85.208	72.523	58.568
G_R (GPa)	80.554	66.730	53.057
G_H (GPa)	82.881	69.627	55.810
E_V (GPa)	198.526	190.909	153.074
E_R (GPa)	187.570	176.392	139.844
E_H (GPa)	193.048	183.656	146.477
ν_R	0.165	0.316	0.307
ν_R	0.164	0.322	0.318
ν_H	0.165	0.319	0.312

5. Vibrational properties

The vibrational and dynamical properties are encoded in phonon dispersion of materials [64]. After SFO structural relaxation for GGA-PBE and GGA-PBE + U functionals; we calculate the phonon dispersion and density of states (DOS) using density functional perturbation theory (DFPT) [65,66]. The phonon calculations have been carried out for the entire BZ with a 5 × 5 × 4 Monkhorst Pack grid k-points mesh without considering any symmetry restriction. The plane wave energy cut-off is set to 520 eV. The symmetry for orthorhombic SFO with *Pbnm* space group dictates 24 Raman active ($\Gamma_{\mathrm{Raman}} = 7A_g + 5B_{1g} + 7B_{2g} + 5B_{3g}$), 25 infrared active ($\Gamma_{\mathrm{IR}} = 7B_{1u} + 9B_{2u} + 9B_{3u}$), [24]8 silent ($8A_u$) and 3 acoustic ($1B_{1u} + 1B_{2u} + 1B_{3u}$); in total of 60 modes at the Γ-point in the BZ center [30,67]. This is consistent with the fact that the SFO three-dimensional ($d = 3$) unit cell has $n = 20$ atoms and lattice vibration theory dictates the presence of $3n = 60$ phonon modes; out of which three are acoustic and the remaining $3n - d = 57$ modes are optical at Γ-point for both GGA-PBE and GGA-PBE + U, see Fig. 2 (a), (b). The three acoustic modes describe the translational motion of atoms as a whole are degenerate at Γ-point (as $k \to 0$) and the dynamical stability of the orthorhombic SFO is evident from the absence of any imaginary phonon frequencies in the entire BZ for both GGA-PBE and GGA-PBE + U. Atoms with heavy (Sm), moderate (Fe) and light (O) masses are expected to dominate over lower, moderate and higher wave number ranges.

This is evident as dominant contributions from Sm, Fe and O are in 50–150 cm^{-1}, 150–300 cm^{-1} and 250–550 cm^{-1} wave number range respectively, see right columns in Fig. 2 (a), (b). Inspired by the work of Paudel *et al.* in Ref. [68], we correlate the peaks in phonon TDOS for GGA-PBE and GGA-PBE + U with the experimentally observed Raman peaks in Ref. [30], see Table 6. Based on the group theoretic discussion in Refs. [27,67], Raman active phonon modes in the lower wave number below 200 cm^{-1} have originated from Sm–O bond stretching, the FeO_6 octahedral motion contributes in 200–350 cm^{-1}, while in the 350–500 cm^{-1} range phonon modes originate from the bending motion and beyond 500 cm^{-1} Fe–O stretching motion produces the phonon peaks.

6. Born effective charge

The Born effective charge (BEC) is an important quantity which mediates the screening of Coulomb interaction between the nuclei and plays an important role in determining the phonon dispersion for polar materials [69,70]. The emergence of ferroelectric behavior in non-polar orthorhombic SFO is debatable and requires detail theoretical investigations [23,71]. The electric polarization in a material is intimately related with movement of electric charge in response to perturbation in atomic displacements. The BEC defines the strength of charge flow with respect to this atomic displacement [72]. Usually, large anomalies in BEC as compared the nominal atomic charges often indicate emergence of ferroelectric behavior in polar materials. The BEC tensor is calculated for GGA-PBE and GGA-PBE + U, see Table 7. The nominal charges of Sm, Fe and O are defined by their 3 + , 3+ and 2− valence states in a closed shell ionic picture where Sm and Fe are electron donor and O acts as electron acceptor. The average BEC calculated from the diagonal elements of the charge tensor are 3.978 (3.71), 5.094 (3.962), 3.015 (2.554) and 3.042 (2.569) for Sm, Fe, O1 and O2 calculated from GGA-PBE (GGA-PBE + U) respectively. The values of BEC obtained from GGA-PBE + U provide better agreement with the nominal charges than that of GGA-PBE. No large anomalies are observed for Sm, Fe and O in

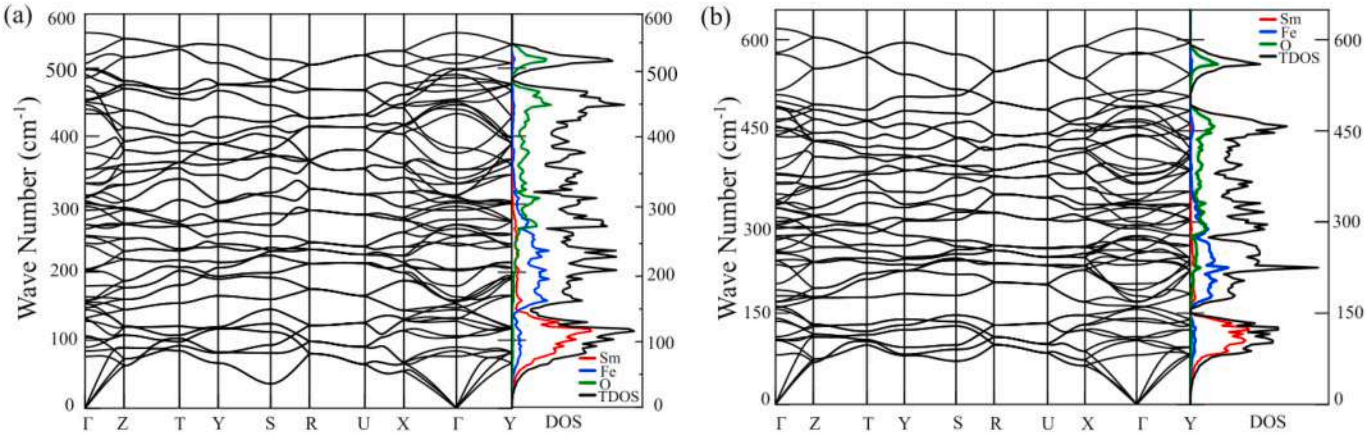

Fig. 2. Phonon band structure, total density of states TDOS and partial density of states PDOS for Sm, Fe and O atoms (in right column) using the DFPT for (a) GGA-PBE, (b) GGA-PBE + U functionals. The phonon dispersion curves in the band structure are plotted along the high symmetry k-points Γ, R, S, T, U, Y and Z in SFO Brillouin zone.

Table 6

Comparison among peak positions in phonon TDOS calculated by DFPT for GGA-PBE and GGA-PBE + U and experimentally obtained values of Raman peaks in SFO [30].

Phonon ModeAssignment	GGA-PBE (cm^{-1})	GGA-PBE + U (cm^{-1})	Exp. Values (cm^{-1})	Main Atomic Motion
A_g	102.9	108.19	104	Sm–O Stretching
B_{1g}	–	118.69	119	Sm–O Stretching
B_{3g}	129.47	130.48	128	Sm–O Stretching
A_g	–	138.31	137	Sm–O Stretching
B_{1g}	142.63	–	–	Sm–O Stretching
B_{2g}	162.66	–	152	Sm–O Stretching
A_g	229.05	212.19	223	FeO_6, bending, stretching
B_{3g}	239.01	234.47	238	
B_{1g}	291.86	300.67	290	
A_g	311.92	308.75	310	O–Fe–O, rotation, stretching
B_{2g}	341.92	345.89	345	
B_{1g}	351.92	–	347	FeO_6, bending, stretching
A_g	358.30	364.84	–	O–Fe–O, rotation, bending
B_{3g}	374.62	375.37	320	
B_{1g}	404.96	406.18	405	FeO_6, rotation, stretching
B_{3g}	428.23	431.41	425	O–Fe–O, rotation, bending
B_{2g}	437.85	438.75	–	
A_g	461.43	460.59	459	O–Fe–O, rotation, bending
B_{1g}	481.35	479.66	486	FeO_6, antisymmetric stretching
B_{2g}	–	–	494	
B_{3g}	–	527.54	521	
A_g	547.52	587.30	562	Fe–O stretching
B_{1g}	–	–	–	Fe–O stretching
B_{2g}	–	–	634	

the BEC tensor calculated for GGA-PBE + U. This is consistent with the fact that collinear G-AFM SFO in *Pbnm* structure is non-polar. The small deviations in BEC from the nominal atomic charge bear the signature of a small covalence effect. Moreover, the presence of small off-diagonal elements and small anisotropy in the diagonal elements for the O sites can be attributed to the covalent nature of the bonding between O-2*p* and Fe-3*d* orbitals [73].

7. Electronic properties

To analyze the electronic properties of SFO, we calculate the spin-resolved total density of states (TDOS) as a function of energy with a 14 eV energy window centered at the Fermi level (E_F) for different exchange-correlation functionals, see Fig. 3. Although the LDA and semi-local GGA-PBE are computationally cheaper in comparison with more sophisticated methods, they result in non-zero TDOS at E_F indicating a metallic behavior for G-AFM SFO, see Fig. 3 (a, b). In case of LDA similar metallic behavior for SFO can be found in Refs. [31,32]. But this metallic state of SFO is inconsistent with experimentally measured electrically resistive nature of orthorhombic *Pbnm* SFO up to the Neel temperature $T_N = 670$ K [23,74]. This discrepancy in case of LDA and GGA-PBE can be attributed to inadequate description of strong Coulomb repulsion between the electrons in localized partially filled *d* (in Fe) and *f* orbitals (in Sm) in SFO. The on site Hubbard U interaction term in case of LDA + U opens up a gap of 1.86 eV between the highest occupied (highest occupied molecular orbital, HOMO) and lowest unoccupied (lowest unoccupied molecular orbital, LUMO) energies in TDOS at the Fermi level; see Fig. 3 (c) which is consistent with the results obtained from DFT simulation using a different software package (ABINIT) [33,75]. In case of the semi local GGA-PBE + U, the insulating energy gap is found to be 2 eV in Fig. 3 (d). The Hubbard U term for both LDA + U and GGA-PBE + U is a semiempirical parameter that needs to be optimized depending on the type of materials. The choice of material dependent U parameter is usually ad-hoc in nature. A more systematic and rigorous method, such as mBJ, can be found by climbing one step in the Jacob's ladder with increased computational complexity [76,77]. The mBJ is usually used in combination with the LDA where the LDA exchange potential is replaced by the mBJ potential leaving the electron correlation potential unchanged [52]. Here we implement the mBJ on top of GGA-PBE, i.e., the GGA-PBE exchange is treated with mBJ leaving the electron correlation unchanged. The mBJ exchange potential has outperformed basic LDA and GGA-PBE in electronic structure calculations and provides more accurate DOS and bandgap for different semiconducting and insulating materials [78–80]. In our calculation this is evident from the fact that mBJ resulted in 2 eV energy gap in TDOS around E_F similar to the GGA-PBE + U methods, see Fig. 3 (e). Now we climb one more step in the Jacob's rung and implement the HSE06 hybrid functional in which only the exchange interaction of the GGA-PBE is divided into short- and long-range parts leaving the electron correlation part unchanged. The 25% of the short range GGA-PBE exchange is replaced by the exact Hartree–Fock exchange with screening parameter $\mu = 0.2\ \mathring{A}^{-1}$ for the inter electronic Coulomb potential. This empirical screening parameter defines the interaction range to be $2/\mu =$

Table 7
Calculated Born effective charge tensor for GGA-PBE and GGA-PBE + U for orthorhombic SFO in G-AFM configuration.

	Z_B	Position	xx	yy	zz	xy	xz	yx	yz	zx	zy
GGA-PBE	Sm	4a	4.100	4.076	3.759	−0.318	0.000	−0.270	0.000	0.000	0.000
	Fe	4b	4.819	5.286	5.179	0.187	0.199	−0.090	−0.170	−0.116	−0.065
	O1	8d	−3.075	−3.516	−2.455	0.746	0.084	0.661	−0.168	0.341	−0.171
	O2	4c	−2.769	−2.329	−4.027	−0.182	0.000	−0.448	0.000	0.000	0.000
GGA-PBE + U	Sm	4a	3.768	3.707	3.656	−0.208	0.000	−0.188	0.000	0.000	0.000
	Fe	4b	3.873	4.022	4.012	0.245	0.305	−0.131	−0.090	−0.2216	−0.1005
	O1	8d	−2.706	−2.871	−2.087	0.648	0.096	0.644	−0.094	0.059	−0.085
	O2	4c	−2.227	−1.987	−3.495	0.106	0.000	0.008	0.000	0.000	0.000

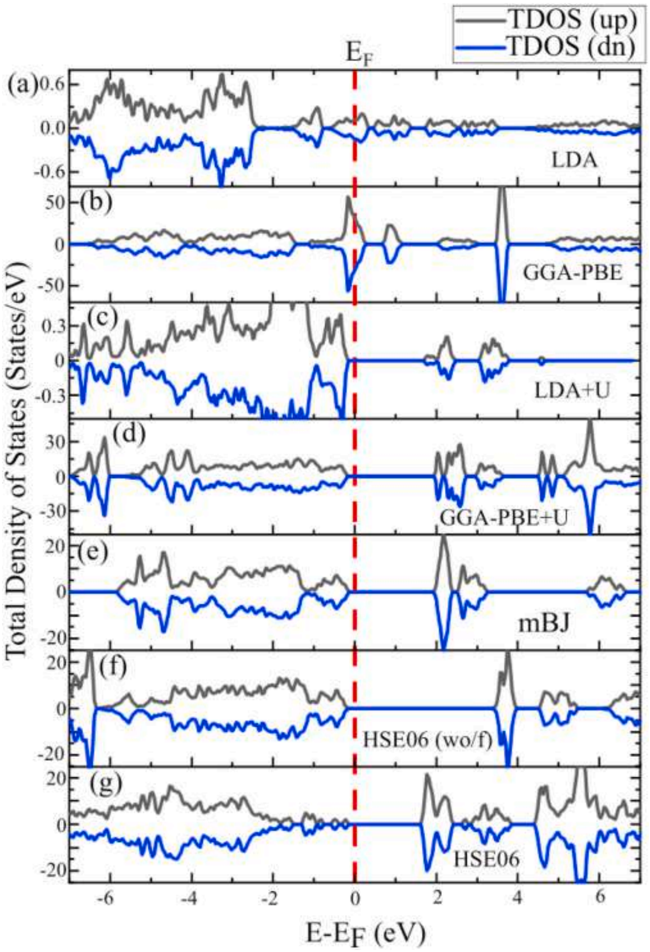

Fig. 3. Total density of states TDOS of orthorhombic SFO calculated with (a) LDA, (b) GGA-PBE, (c) LDA + U, (d) GGA-PBE + U, (e) mBJ, (f) HSE06 with Sm-4*f* orbital in core, (g) HSE06 with Sm-4*f* orbital in valence for PAW method. Due to AFM ordering, symmetry exists between the spin-up in the upper part and and spin-down in the lower part of the TDOS. The red dashed line indicates the position of the Fermi level E_F. (For interpretation of the references to colour in this figure legend, the reader is referred to the Web version of this article.)

10 nm which is short ranged over a few neighbors at proximity [81].

Now within the HSE06 framework, treating the Sm-4*f* electrons as valence imposes significant computational complexities in structural relaxation and self-consistent energy calculations. At first, we treat the Sm-4*f* electron as a core to keep the computational complexities and convergence issues manageable and found a 3.42 eV gap around the E_F in TDOS which significantly higher than all other methods mentioned above, see Fig. 3 (f). Although the phonon frequency and density of states in rare earth ortho ferrites are shown to have small effect whether the Sm-4*f* electrons are treated as core or valence [27]; electronic density of states are expected to depend on it. Hence, we implement the HSE06 treating the Sm-4*f* electrons as valence with higher computation cost and obtained 1.73 eV energy gap, see Fig. 3 (g); which is much smaller compared to the case when Sm-4*f* electrons are treated as core in PAW method above.

To analyze the structure of the density of states, we projected the TDOS onto the atomic orbitals of individual ions in SFO and calculate the partial density of states (PDOS) of Sm, Fe and O. First, we present the PDOS for the semi local GGA-PBE to show explicitly why it fails to predict the insulating nature of SFO. It is evident that significant contributions in the density of states are coming from localized the Sm-4*f* and the Fe-3*d*; and also, from the O-2*p* orbitals and mixing occurs between these orbitals at E_F, see Fig. 4 (c), (e) and (f). This embodies the fact that GGA-PBE exchange-correlation functional incorrectly models the electron interactions between these states. The semi-local GGA-PBE delocalize the *f* and *d* orbitals electrons excessively in SFO which results in orbital instability leading to the false metallic nature. This excess charge density delocalization is usually attributed to uncompensated electron self-interaction and improper modelling for non-local exchange interaction [82].

The Hubbard U correction term for GGA-PBE + U tends to improve the *d* and *f* orbital stabilization and correctly predict the insulating state, see Fig. 5. Although GGA-PBE + U is widely used for transition and rare-earth materials for its reasonable computational requirements, the

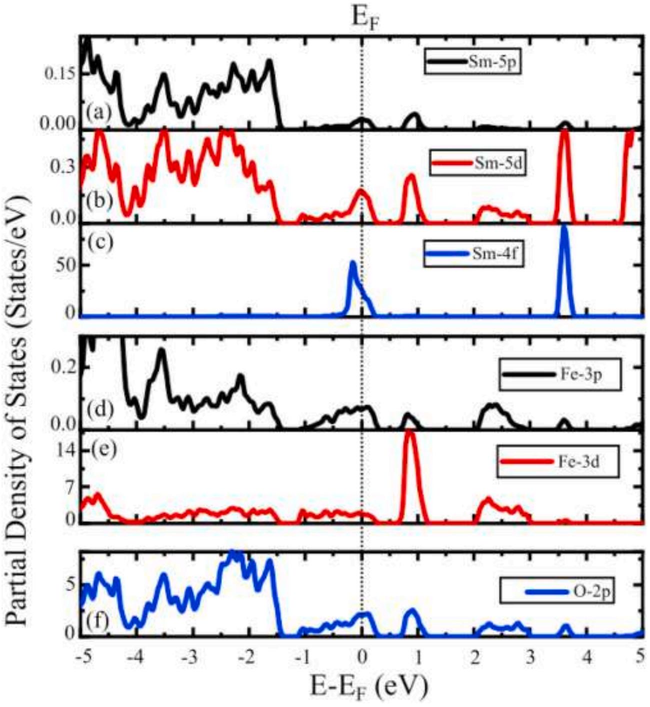

Fig. 4. Partial density of states PDOS by projecting TDOS on to (a), Sm-5*p*, (b) Sm-5*d*, (c) Sm-4*f*, (d) Fe-3*p*, (e) Fe-3*d* and (f) O-2*p* for GGA-PBE. Due to the AFM spin symmetry considerations, only PDOS for up spin channel is plotted for clarity.

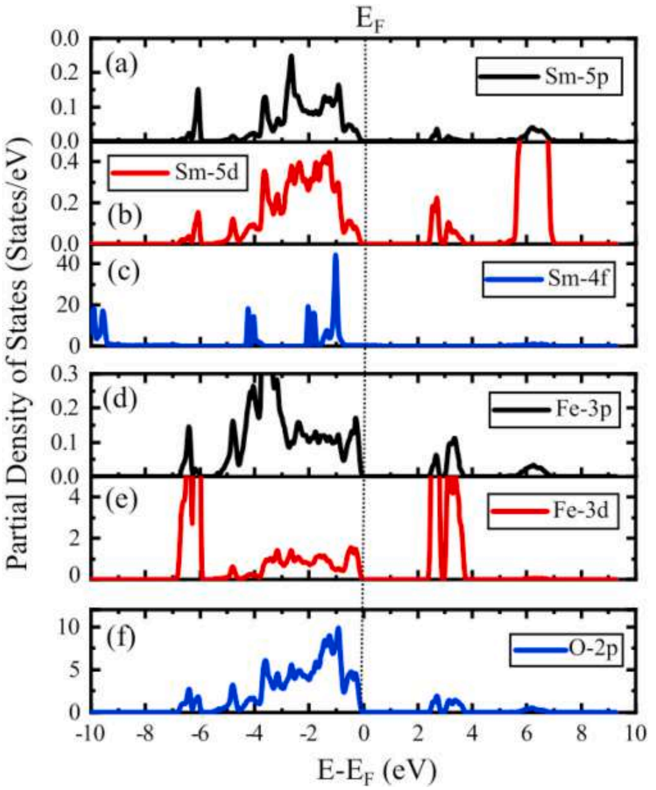

Fig. 5. Partial density of states PDOS by projecting TDOS on to (a), Sm-5*p*, (b) Sm-5*d*, (c) Sm-4*f*, (d) Fe-3*p*, (e) Fe-3*d* and (f) O-2*p* for GGA-PBE + U.

choice of the U is orbital specific, and often empirically set to match the experimental values. The self-consistent calculations of U to avoid ambiguities can often be limited to simple materials [83].

The hybrid functional just has one empirical parameter defining the mixing of non-local HF exchange. Its value is set to be 25% based on solid theoretical calculations within the framework of perturbation theory [84,85]. Moreover, the success of HSE06 functional in describing the *d* and *f* orbitals in RFeO$_3$ is well established [82,86–88]. Here we present HSE06 hybrid functional based calculations to explain the detail electronic structure of the SFO.

From −10 to −2 eV, significant amount of mixing occurs between Sm-4*f*, Fe-3*d*, and O-2*p* resulting strong hybridization among these states, see Fig. 6 (c), (e) and (f). Near the top-of the valence band (VB) within the energy window of −2 to 0 eV (E$_F$), energy bands are almost exclusively derived from hybridization between Fe-3*d* and O-2*p* states. The bottom of the conduction band is formed due to mixing between Sm-4*f*, Fe-3*d* and O-2*p* states around 2 eV. As we go higher in energy, around 3 eV, the mixing occurs among dominant Fe-3*d*, small Sm-4*f* and O-2*p* states. From 4 to 10 eV energy range, the DOS originates from Sm-4*f*, Sm-5*d*, Fe-3*d* and O-2*p* states.

We perform electronic band structure calculations using HSE06 along the high symmetry directions *Γ*, X, R, S, T, U, Y, and Z in the Brillouin zone of the orthorhombic SFO within the energy range from −10 to 10 eV centered at E$_F$, see Fig. 7. The valence band maximum and the conduction band minimum occur at R point indicating a direct bandgap of 1.75 eV for SFO. It is interesting to note that energy levels near the bottom of the CB have small dispersion which can be attributed to the fact that localized Sm-4*f* and Fe-3*d* orbitals mostly responsible for constructing those bands. The dispersion near the top of the valence band is more pronounced which resembles the presence of spatially delocalized O-2*p* states.

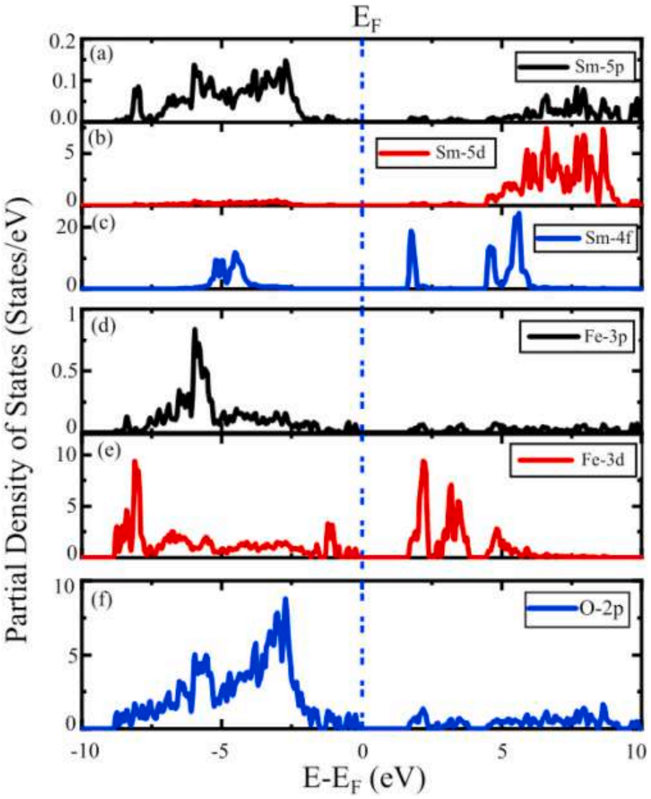

Fig. 6. Spin resolved PDOS by projecting onto Partial density of states PDOS by projecting TDOS on to (a), Sm-5*p*, (b) Sm-5*d*, (c) Sm-4*f*, (d) Fe-3*p*, (e) Fe-3*d* and (f) O-2*p* for HSE06 hybrid functional with Sm-4*f* electrons treated as valence in PAW method.

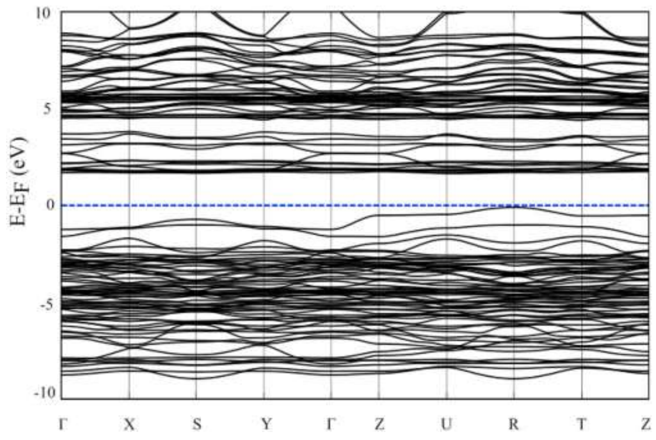

Fig. 7. Electronic band structure along high symmetry k-points *Γ*, R, S, T, U, Y and Z in the orthorhombic SFO Brillouin zone for HSE06 hybrid functional.

8. Optical properties

The optical behavior codifies many important characteristics about the materials such as electronic energy bands and vibrational phonon modes [89,90]. The frequency dependent complex dielectric constant $\epsilon(\omega) = \epsilon_{\text{real}}(\omega) + i\epsilon_{\text{imag}}(\omega)\left(i = \sqrt{-1}\right)$ serves as an important experimental tool to probe energy band structure of the material. We used the Fermi's golden rule to calculate the imaginary part ϵ_{imag} of the complex ϵ [91–93]. The dipole transition matrix elements required in obtaining ϵ_{imag} are estimated from the electronic band structure simulations using GGA-PBE + U functional. The real part ϵ_{real} is estimated from ϵ_{imag} using well known Kramer-Kronig relations. The quantities like absorption coefficient α, reflectivity R, energy loss function L, refractive index η, extinction coefficient K, and optical conductivity σ are derived from estimated ϵ using standard relation and all these quantities defines the linear optical response [90]. During the simulations, we considered three orthogonal polarization along x, y and z direction denoted as E_x, E_y and E_z.

In the static limit $\omega \rightarrow 0$, the ϵ_{real} and ϵ_{imag} attained different values for E_x, E_y and E_z, as shown in Fig. 8 (a, b). This indicates the presence of optical anisotropy in SFO. The degree of anisotropy in the real dielectric constant can be estimated by comparing the ϵ_{real} for two different polarization directions; for example, the ratio of $\epsilon^{yy}_{real}(3.90)$ to $\epsilon^{zz}_{real}(3.82)$ which is 1.021. The average value of the ϵ_{real} is 3.81. The maxima for ϵ_{real} occur at 2.81 eV, 2.75 eV and 3.29 eV for E_x, E_y and E_z respectively. The imaginary part ϵ_{imag} encodes optical absorption characteristics of the material. The estimated energy cutoff E_c for ϵ_{imag} is about 2 eV which is at resonance with the estimated bandgap of the SFO using GGA-PBE + U, see Fig. 5. The ϵ_{imag} also exhibits optical anisotropies for three polarizations and its maxima appeared at 3.66 eV, 3.54 eV and 3.63 eV for E_x, E_y and E_z respectively. The presence of a number of peaks in ϵ_{imag} within the energy window [0 eV, 10 eV] are due to electronic transitions between different orbitals in SFO. The absorption peak at 3.66 eV can be attributed to interband transition between O-2*p* valence bands and Fe-3*d* conduction bands. Below the bandgap energy of 2 eV, $\alpha \rightarrow 0$ signifies no

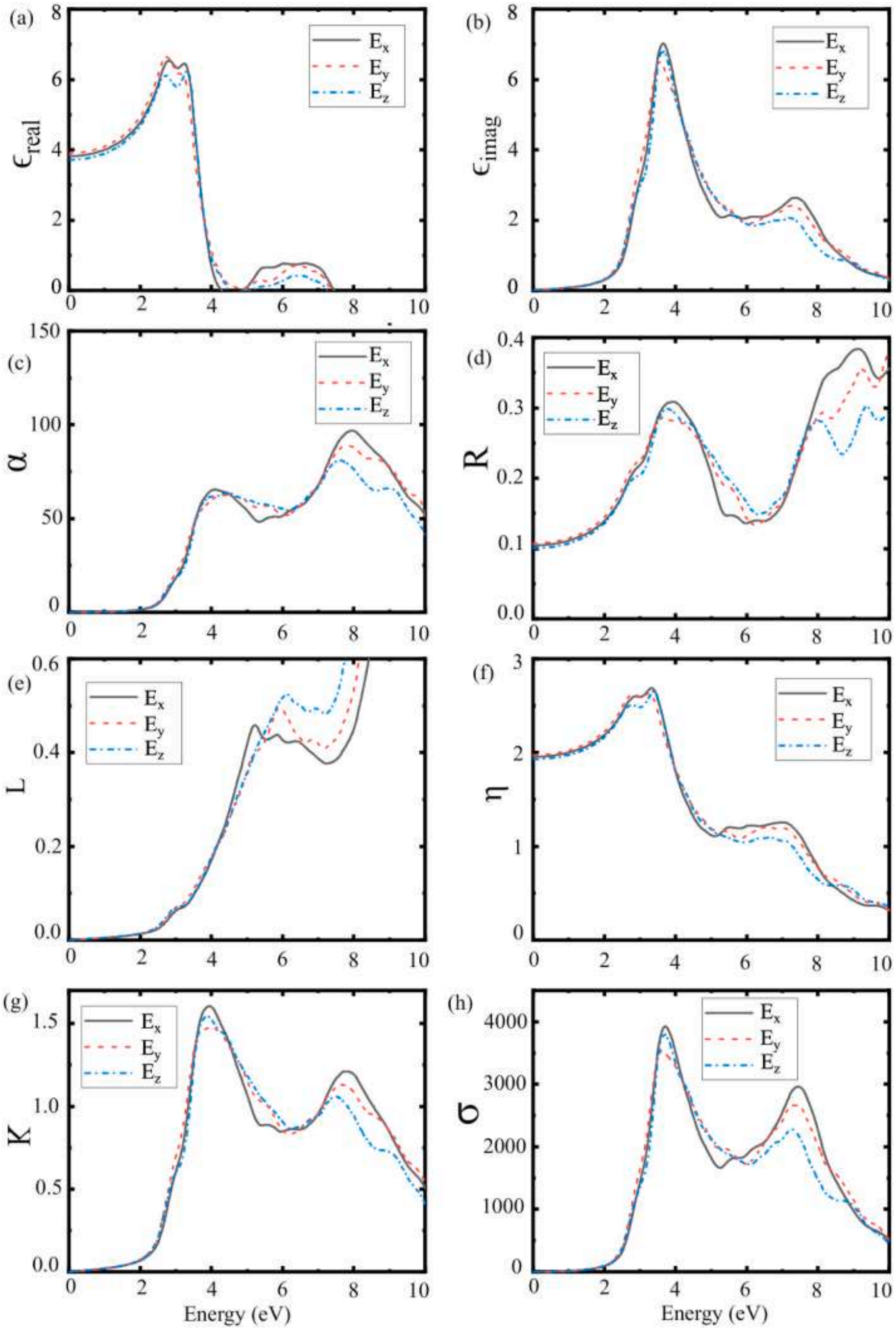

Fig. 8. Optical properties (a) real part of dielectric constant ϵ_{real}, (b) Imaginary part of dielectric constant ϵ_{imag}, (c) Absorption coefficient α, (d) Reflectance R, (e) Loss function L, (f) Refractive index η, (g) Extinction coefficient K, (h) Optical conductivity σ as a function of photon energy E calculated from GGA-PBE + U for three different polarizations E_x, E_y and E_z.

optical absorption occurring in SFO; whereas above 2 eV significant optical absorption occurs up to 10 eV with two strong peaks around 4.11 eV and 7.98 eV, see.

Fig. 8 (c). In the static limit, the reflectivity R has three different values 10.42%, 10.74% and 10.04% for E_x, E_y and E_z respectively, see Fig. 8 (d). The *R* has its maximum value of 38.37% at 9.14 eV for E_x; for E_x and E_z it attains 35.48% and 30.19% at 9.25 eV and 9.36 eV respectively. To quantify losses in SFO, the energy loss function L is plotted in Fig. 8 (e). The optical losses sharply increase from zero starting from the bandgap of SFO and the peak at 6.04 eV for E_z signifies the plasmon resonance [52]. In the $\omega \rightarrow 0$ limit, the refractive index η has an average value of 1.95 obtained from its 1.95, 1.97 and 1.92 values for E_x, E_y and E_z, see Fig. 8 (f). The extinction coefficient K goes to zero below the bandgap energy and increases for energies higher than bandgap as shown in Fig. 8 (g). The maximum attenuation occurs at 3.94 eV, 3.97 eV and 3.86 eV for E_x, E_y and E_z respectively. The optical conductivity σ is related with the dielectric constant as $\sigma = \omega\epsilon_{\text{imag}}$; and has similar features in as shown in see Fig. 8 (h). The σ vanishes below the 2 eV bandgap indicating absence of optically generated carrier in SFO and has two distinct peaks similar to ϵ_{imag}.

9. Conclusion

We have studied structural, elastic, vibrational, electronic and optical properties of orthorhombic SFO using the PAW method within the framework of DFT. First principles calculations have been performed to estimate the total energies for different possible magnetic configurations and found G-AFM to be the ground state with minimum energy which is consistent with experimental observations. We have calculated the lattice parameters, atomic positions, relevant ionic radii, bond lengths and bond angles for SFO for a number of standard exchange-correlation functionals and made a comparative study among them. We simulated the elastic properties of SFO in terms standard parameters like different elastic constants and moduli; and demonstrated the mechanical stability of the orthorhombic SFO. The dynamical stability of SFO has been confirmed from the phonon mode analysis using DFPT. The peaks in our theoretical phonon TDOS are compared with experimental observations. We estimated the effective born charges for orthorhombic SFO. For electronic properties analysis, simulations have been performed using different approximations in the Jacob's ladder for the exact exchange-correlation functional and detail discussions are presented for comparative analysis. We found mBJ and HSE06 hybrid functional to provide better model for the localized *d* and *f* orbitals in SFO as expected for rare-earth materials. Finally, the optical properties are simulated using Fermi's golden rule for GGA-PBE + U functional. The theoretical investigations presented here favor the GGA-PBE + U as a preferred functional for SFO in explaining structural, elastic, vibrational, electronic and optical properties with reasonable accuracy and computational cost.

Author contributions

S.A. and S.S.N. contributed equally. I.A. and A.K. planned the project. S.A., S.S.N., A.K.M.S.H.F., T.H. and S.C. performed the simulations. S.A., S.S.N. and I.A. analyzed the data. All authors contributedin the writing of the manuscript.

Declaration of competing interest

The authors declare that they have no known competing financial interests or personal relationships that could have appeared to influence the work reported in this paper.

Acknowledgments

We gratefully acknowledge Dr. Tapas Debnath, Department of Theoretical and Computational Chemistry, University of Dhaka for providing the license for the Vienna *Ab Initio* Simulation Package (VASP). We are also very thankful to Dr. Shafiul Alam, Department of Electrical and Electronic Engineering, University of Dhaka for the access to high-performance computing facility.

References

[1] R. White, Review of recent work on the magnetic and spectroscopic properties of the rare-earth orthoferrites, J. Appl. Phys. 40 (1969) 1061–1069.

[2] R.M. Bozorth, Origin of weak ferromagnetism in rare-earth orthoferrites, Phys. Rev. Lett. 1 (1958) 362.

[3] D. Treves, Magnetic studies of some orthoferrites, Phys. Rev. 125 (1962) 1843.

[4] T. Yamaguchi, K. Tsushima, Magnetic symmetry of rare-earth orthochromites and orthoferrites, Phys. Rev. B 8 (1973) 5187.

[5] S. Cao, H. Zhao, B. Kang, J. Zhang, W. Ren, Temperature induced spin switching in $SmFeO_3$ single crystal, Sci. Rep. 4 (2014) 5960.

[6] A.P.B. Selvadurai, R. Thiyagarajan, V. Pazhanivelu, R. Suriakarthick, W. Yang, R. Murugaraj, C. Venkateswaran, Metamagnetism emergence and spectroscopic elucidation of $SmFeO_3$ nanoceramics, J. Phys. D Appl. Phys. 52 (2019) 435002.

[7] S. Chaturvedi, P. Shyam, R. Bag, M.M. Shirolkar, J. Kumar, H. Kaur, S. Singh, A. M. Awasthi, S. Kulkarni, Nanosize effect: enhanced compensation temperature and existence of magnetodielectric coupling in $SmFeO_3$, Phys. Rev. B 96 (2017), 024434.

[8] A. Ahlawat, S. Kushwaha, A.A. Khan, S. Satapathy, R.J. Choudhary, A.K. Karnal, Influence of particle size on spin switching properties and magnetoelectric coupling in $SmFeO_3$, J. Mater. Sci. Mater. Electron. 29 (2018) 927–934.

[9] X. Wang, X. Cheng, S. Gao, J. Song, K. Ruan, X. Li, Room temperature exchange bias in $SmFeO_3$ single crystal, J. Magn. Magn Mater. 399 (2016) 170–174.

[10] X. Fu, X. Zeng, D. Wang, H.C. Zhang, J. Han, T.J. Cui, Ultralow temperature terahertz magnetic thermodynamics of perovskite-like $SmFeO_3$ ceramic, Sci. Rep. 5 (2015) 14777.

[11] M. Abe, K. Kaneta, M. Gomi, Y. Mori, S. Nomura, Magnetostriction of $SmFeO_3$ and $YFe_{1\text{-}x}Co_{x/2}Ti_{x/2}O_3$ in the spin reorientation region, J. Appl. Phys. 16 (1977) 1799.

[12] Z. Zhou, L. Guo, H. Yang, Q. Liu, F. Ye, Hydrothermal synthesis and magnetic properties of multiferroic rare-earth orthoferrites, J. Alloys Compd. 583 (2014) 21–31.

[13] A. Ahlawat, S. Satapathy, R.J. Choudhary, M.M. Shirolkar, M.K. Singh, P.K. Gupta, Tunable room temperature magnetoelectric response of $SmFeO_3$/poly (vinylidene fluoride) nanocomposite films, RSC Adv. 6 (2016) 44843–44850.

[14] J. Liu, E. Sheha, S.I. El-Dek, D. Goonetilleke, M. Harguindeguy, N. Sharma, "$SmFeO_3$ and Bi-doped $SmFeO_3$ perovskites as an alternative class of electrodes in lithium-ion batteries", CrystEngComm 20 (2018) 6165–6172.

[15] B.V. Prasad, G.N. Rao, J.W. Chen, D.S. Babu, "Abnormal high dielectric constant in $SmFeO_3$ semiconductor ceramics", Mater. Res. Bull. 46 (2011) 1670–1673.

[16] A.A. Khan, S. Satapathy, A. Ahlawat, P. Deshmukh, A.K. Karnal, "Magneto-dielectric coupling in $SmFeO_3$: a study on anomalous dielectric, conductivity, impedance at spin reorientation temperature", Ceram. Int. 44 (2018) 12401–12413.

[17] P. Tang, D. Ni, F. Cao, B. Li, "Microwave synthesis of nanoparticulate $SmFeO_3$ and its characterization", J. Nanosci. Nanotechnol. 16 (2016) 1151–1154.

[18] R. Maity, A.P. Sakhya, A. Dutta, T.P. Sinha, "Investigation of concentration dependent electrical and photocatalytic properties of Mn doped $SmFeO_3$", Mater. Chem. Phys. 223 (2019) 78–87.

[19] C. Zhang, M. Shang, M. Liu, T. Zhang, L. Ge, H. Yuan, S. Feng, "Multiferroicity in $SmFeO_3$ synthesized by hydrothermal method", J. Alloys Compd. 665 (2016) 152–157.

[20] J. Liu, M. Niu, L. Wang, G. Chen, D. Xu, "Structure, ferroelectric and magnetic characteristics of $SmFeO_3$ and $BaTiO_3$ co-modified $BiFeO_3$ ceramics", J. Mater. Sci. Mater. Electron. 31 (2020) 3479–3491.

[21] R.O. Jones, Density functional theory: its origins, rise to prominence, and future, Rev. Mod. Phys. 87 (2015) 897.

[22] H.J. Zhao, J. Íñiguez, X.M. Chen, L. Bellaiche, Origin of the magnetization and compensation temperature in rare-earth orthoferrites and orthochromates, Phys. Rev. B 93 (2016), 014417.

[23] J.-H. Lee, Y.K. Jeong, J.H. Park, M.-A. Oak, H.M. Jang, J.Y. Son, J.F. Scott, "Spin-Canting-Induced improper ferroelectricity and spontaneous magnetization reversal in $SmFeO_3$", Phys. Rev. Lett. 107 (2011) 117201.

[24] R.D. Johnson, N. Terada, P.G. Radaelli, "Comment on "spin-canting-induced improper ferroelectricity and spontaneous magnetization reversal in $SmFeO_3$", Phys. Rev. Lett. 108 (2012) 219701.

[25] J.-H. Lee, Y.K. Jeong, J.H. Park, M.-A. Oak, H.M. Jang, J.Y. Son, J.F. Scott, Lee et al. Reply, Phys. Rev. Lett. 108 (2012) 219702.

[26] C.-Y. Kuo, Y. Drees, M.T. Fernandez-Diaz, L. Zhao, L. Vasylechko, D. Sheptyakov, A.M.T. Bell, T.W. Pi, H.-J. Lin, M.-K. Wu and others, "k= 0 magnetic structure and absence of ferroelectricity in $SmFeO_3$", Phys. Rev. Lett. 113 (2014) 217203.

[27] M.C. Weber, M. Guennou, H.J. Zhao, J. Íñiguez, R. Vilarinho, A. Almeida, J. A. Moreira, J. Kreisel, "Raman spectroscopy of rare-earth orthoferrites $RFeO_3$ (R= La, Sm, Eu, Gd, Tb, Dy)", Phys. Rev. B 94 (2016) 214103.

[28] S. Tyagi, V.G. Sathe, G. Sharma, M.K. Gupta, R. Mittal, V. Srihari, H.K. Poswal, “Detail investigations of $SmFeO_3$ under extreme condition”, Mater. Chem. Phys. 215 (2018) 393–403.

[29] V.S. Bhadram, B. Rajeswaran, A. Sundaresan, C. Narayana, “Spin-phonon coupling in multiferroic $RCrO_3$ (Ry, Lu, Gd, Eu, Sm): a Raman study”, Europhys. Lett. 101 (2013) 17008.

[30] S. Gupta, R. Medwal, S.P. Pavunny, D. Sanchez, R.S. Katiyar, “Temperature dependent Raman scattering and electronic transitions in rare earth $SmFeO_3$”, Ceram. Int. 44 (2018) 4198–4203.

[31] M. Iglesias, A. Rodriguez, P. Blaha, V. Pardo, D. Baldomir, M. Pereiro, J. Botana, J. E. Arias, K. Schwarz, Ab initio electronic structure of rare earth orthoferrites, J. Magn. Magn Mater. 290 (2005) 396–399.

[32] N. Singh, J.Y. Rhee, S. Auluck, “Electronic and magneto-optical properties of rare-earth orthoferrites $RFeO_3$ (R= Y, Sm, Eu, Gd and Lu)”, J. Kor. Phys. Soc. 53 (2008) 806–811.

[33] V.V. Triguk, I.I. Makoed, A.F. Ravinski, Electronic structure and improper electric polarization of samarium orthoferrite, Phys. Solid State 58 (2016) 2443–2448.

[34] G. Kresse, J. Furthmüller, Efficient iterative schemes for ab initio total-energy calculations using a plane-wave basis set, Phys. Rev. B 54 (1996) 11169.

[35] G. Kresse, D. Joubert, From ultrasoft pseudopotentials to the projector augmented-wave method, Phys. Rev. B 59 (1999) 1758.

[36] W. Kohn, L.J. Sham, Self-consistent equations including exchange and correlation effects, Phys. Rev. 140 (1965) A1133.

[37] D.M. Ceperley, B.J. Alder, Ground state of the electron gas by a stochastic method, Phys. Rev. Lett. 45 (1980) 566.

[38] J.P. Perdew, J.A. Chevary, S.H. Vosko, K.A. Jackson, M.R. Pederson, D.J. Singh, C. Fiolhais, Atoms, molecules, solids, and surfaces: applications of the generalized gradient approximation for exchange and correlation, Phys. Rev. B 46 (1992) 6671.

[39] J.P. Perdew, M. Ernzerhof, K. Burke, Rationale for mixing exact exchange with density functional approximations, J. Chem. Phys. 105 (1996) 9982–9985.

[40] J.P. Perdew, A. Ruzsinszky, G.I. Csonka, O.A. Vydrov, G.E. Scuseria, L. A. Constantin, X. Zhou, K. Burke, Restoring the density-gradient expansion for exchange in solids and surfaces, Phys. Rev. Lett. 100 (2008) 136406.

[41] S.L. Dudarev, G.A. Botton, S.Y. Savrasov, C.J. Humphreys, A.P. Sutton, Electron-energy-loss spectra and the structural stability of nickel oxide: an LSDA+ U study, Phys. Rev. B 57 (1998) 1505.

[42] V.I. Anisimov, J. Zaanen, O.K. Andersen, Band theory and mott insulators: hubbard U instead of stoner I, Phys. Rev. B 44 (1991) 943.

[43] L. Chen, T. Li, S. Cao, S. Yuan, F. Hong, J. Zhang, “The role of 4f-electron on spin reorientation transition of $NdFeO_3$: a first principle study”, J. Appl. Phys. 111 (2012) 103905.

[44] A.F. Ravinski, V.V. Triguk, I.I. Makoed, “Ab Initio calculations of the lattice dynamics and the ferroelectric instability of the $BiFeO_3$ multiferroic”, Phys. Solid State 56 (2014) 1799–1805.

[45] O. Diéguez, O.E. González-Vázquez, J.C. Wojdeł, J. Íñiguez, “First-principles predictions of low-energy phases of multiferroic $BiFeO_3$”, Phys. Rev. B 83 (2011), 094105.

[46] A. Stroppa, M. Marsman, G. Kresse, S. Picozzi, “The multiferroic phase of $DyFeO_3$: an ab initio study”, New J. Phys. 12 (2010), 093026.

[47] F. Tran, P. Blaha, Accurate band gaps of semiconductors and insulators with a semilocal exchange-correlation potential, Phys. Rev. Lett. 102 (2009) 226401.

[48] J. Heyd, G.E. Scuseria, M. Ernzerhof, Hybrid functionals based on a screened Coulomb potential, J. Chem. Phys. 118 (2003) 8207–8215.

[49] A.V. Krukau, O.A. Vydrov, A.F. Izmaylov, G.E. Scuseria, Influence of the exchange screening parameter on the performance of screened hybrid functionals, Phys. Nor. 125 (2006) 224106.

[50] J. Paier, M. Marsman, K. Hummer, G. Kresse, I.C. Gerber, J.G. Ángyán, Screened hybrid density functionals applied to solids, J. Chem. Phys. 124 (2006) 154709.

[51] T. Hahn, H. Wondratschek, Symmetry of crystals: introduction to international tables for crystallography vol. A, Acta Crystallogr. 53 (1997) 252.

[52] X.-H. Zhu, X.-B. Xiao, X.-R. Chen, B.-G. Liu, “Electronic structure, magnetism and optical properties of orthorhombic $GdFeO_3$ from first principles”, RSC Adv. 7 (2017) 4054–4061.

[53] S. Chaturvedi, P. Shyam, A. Apte, J. Kumar, A. Bhattacharyya, A.M. Awasthi, S. Kulkarni, “Dynamics of electron density, spin-phonon coupling, and dielectric properties of SmFe O_3 nanoparticles at the spin-reorientation temperature: role of exchange striction”, Phys. Rev. B 93 (2016) 174117.

[54] Z. Zhang, P. Wu, L. Chen, J. Wang, “Systematic variations in structural and electronic properties of $BiFeO_3$ by A-site substitution”, Appl. Phys. Lett. 96 (2010), 012905.

[55] F. Giustino, Materials Modelling using Density Functional Theory: Properties and Predictions", Oxford University Press, 2014.

[56] X. Wu, D. Vanderbilt, D.R. Hamann, Systematic treatment of displacements, strains, and electric fields in density-functional perturbation theory, Phys. Rev. B 72 (2005), 035105.

[57] S. Shang, Y. Wang, Z.-K. Liu, “First-principles elastic constants of α-and θ-Al_2O_3”, Appl. Phys. Lett. 90 (2007) 101909.

[58] F. Mouhat, F.-X. Coudert, Necessary and sufficient elastic stability conditions in various crystal systems, Phys. Rev. B 90 (2014) 224104.

[59] R. Hill, The elastic behaviour of a crystalline aggregate, Proc. Phys. Soc. 65 (1952) 349.

[60] H. Dong, C. Chen, S. Wang, W. Duan, J. Li, “Elastic properties of tetragonal $BiFeO_3$ from first-principles calculations”, Appl. Phys. Lett. 102 (2013) 182905.

[61] M.K. Yaakob, M.F.M. Taib, M.S.M. Deni, A. Chandra, L. Lu, M.Z.A. Yahya, “First principle study on structural, elastic and electronic properties of cubic $BiFeO_3$”, Ceram. Int. 39 (2013) S283–S286.

[62] R. Shukla, R. Dhaka, S. Dash, S.C. Sahoo, B. Bahera, P.D. Babu, R. Choudhary, A. K. Patra, others, “Structural, dielectric and magnetic properties of Bi–Mn doped $SmFeO_3$”, Ceram. Int. 46 (2020) 8730–8744.

[63] S.F. Pugh, XCII. Relations between the elastic moduli and the plastic properties of polycrystalline pure metals, Philos. Mag. A 45 (1954) 823–843.

[64] S.H. Simon, The Oxford solid state basics, Oxford Univ. Press (2013) 69–107.

[65] S. Baroni, S. De Gironcoli, A. Dal Corso, P. Giannozzi, Phonons and related crystal properties from density-functional perturbation theory, Rev. Mod. Phys. 73 (2001) 515.

[66] F. Giustino, Electron-phonon interactions from first principles, Rev. Mod. Phys. 89 (2017), 015003.

[67] M.K. Singh, H.M. Jang, H.C. Gupta, R.S. Katiyar, “Polarized Raman scattering and lattice eigenmodes of antiferromagnetic $NdFeO_3$”, J. Raman Spectrosc. 39 (2008) 842–848.

[68] T.R. Paudel, W.R.L. Lambrecht, Calculated phonon band structure and density of states and interpretation of the Raman spectrum in rocksalt ScN, Phys. Rev. B 79 (2009), 085205.

[69] S.-G. Ma, T. Gao, S.-C. Li, X.-J. Ma, Y.-H. Shen, T.-C. Lu, Theoretical investigations on the α-LiAlO2 properties via first-principles calculation, Fusion Eng. Des. 113 (2016) 324–330.

[70] W. Zhong, R.D. King-Smith, D. Vanderbilt, Giant LO-TO splittings in perovskite ferroelectrics, Phys. Rev. Lett. 72 (1994) 3618.

[71] U. Chowdhury, S. Goswami, A. Roy, S. Rajput, A.K. Mall, R. Gupta, S.D. Kaushik, V. Siruguri, S. Saravanakumar, S. Israel, others, Origin of ferroelectricity in orthorhombic $LuFeO_3$", Phys. Rev. B 100 (2019) 195116.

[72] L. Xie, J. Zhu, “The electronic structures, born effective charges, and interatomic force constants in $BaMO_3$ (M= Ti, Zr, Hf, Sn): a comparative first-principles study”, J. Am. Ceram. Soc. 95 (2012) 3597–3604.

[73] P. Ravindran, R. Vidya, A. Kjekshus, H. Fjellvåg, O. Eriksson, “Theoretical investigation of magnetoelectric behavior in $BiFeO_3$”, Phys. Rev. B 74 (2006) 224412.

[74] E.N. Maslen, V.A. Streltsov, N. Ishizawa, “A synchrotron X-ray study of the electron density in $SmFeO_3$”, Acta Crystallogr. B 52 (1996) 406–413.

[75] X. Gonze, A brief introduction to the ABINIT software package, Z. für Kristallogr. - Cryst. Mater. 220 (2005) 558–562.

[76] J.P. Perdew, K. Schmidt, others, Density functional theory and its application to materials", Van Doren (2001) 1–20.

[77] J.P. Perdew, A. Ruzsinszky, Fourteen easy lessons in density functional theory, Int. J. Quant. Chem. 110 (2010) 2801–2807.

[78] D.J. Singh, S.S.A. Seo, H.N. Lee, “Optical properties of ferroelectric $Bi_4Ti_3O_{12}$”, Phys. Rev. B 82 (2010) 180103.

[79] D. Koller, F. Tran, P. Blaha, Improving the modified Becke-Johnson exchange potential, Phys. Rev. B 85 (2012) 155109.

[80] S.W. Fan, L.J. Ding, Z.L. Wang, K.L. Yao, Half-metallic ferromagnetism in wurtzite ScM (M= C, Si, Ge, and Sn): ab initio calculations, Appl. Phys. Lett. 102 (2013), 022404.

[81] J. Paier, M. Marsman, G. Kresse, Dielectric properties and excitons for extended systems from hybrid functionals, Phys Rev. B 78 (2008) 121201.

[82] B.G. Janesko, T.M. Henderson, G.E. Scuseria, Screened hybrid density functionals for solid-state chemistry and physics, Phys. Chem. 11 (2009) 443–454.

[83] A. Rohrbach, J. Hafner, G. Kresse, Molecular adsorption on the surface of strongly correlated transition-metal oxides: a case study for CO/NiO (100), Phys. Rev. B 69 (2004), 075413.

[84] J.P. Perdew, K. Burke, M. Ernzerhof, Generalized gradient approximation made simple, Phys. Rev. Lett. 77 (1996) 3865.

[85] A.D. Becke, A new mixing of Hartree–Fock and local density-functional theories, J. Chem. Phys. 98 (1993) 1372–1377.

[86] A. Stroppa, G. Kresse, Unraveling the Jahn-Teller effect in Mn-doped GaN using the Heyd-Scuseria-Ernzerhof hybrid functional, Phys. Rev. B 79 (2009) 201201.

[87] M. Marsman, J. Paier, A. Stroppa, G. Kresse, Hybrid functionals applied to extended systems, J. Phys. Condens. Matter 20 (2008), 064201.

[88] A. Stroppa, S. Picozzi, Hybrid functional study of proper and improper multiferroics, Phys. Chem. Chem. Phys. 12 (2010) 5405–5416.

[89] M. Fox, Optical properties of solids, American Association of Physics Teachers (2002).

[90] M. Dresselhaus, G. Dresselhaus, S.B. Cronin, A.G. Souza Filho, Solid State Properties, Springer, 2018.

[91] I. Merad Boudia, A.H. Reshak, T. Ouahrani, Z. Bentalha, Density functional theory calculation of the optical properties and topological analysis of the electron density of $MBi_2B_2O_7$ (M= Ca, Zn) compounds, J. Appl. Phys. 113 (2013), 083505.

[92] T. Ouahrani, A.H. Reshak, A.O. de La Roza, M. Mebrouki, V. Luaña, R. Khenata, B. Amrani, First-principles study of structural, electronic, linear and nonlinear optical properties of Ga_2PSb ternary chalcopyrite, Eur. Phys. J. B 72 (2009) 361–366.

[93] A.H. Reshak, X. Chen, I.V. Kityk, S. Auluck, Specific features of second order optical susceptibilities for a complex borate crystal $Bi_2ZnB_2O_7$: experiment and theory, Curr. Opin. Solid State Mater. Sci. 11 (2007) 33–39.